Nanoscale

PAPER

View Article Online
View Journal | View Issue

Cite this: *Nanoscale*, 2016, **8**, 12221

Synthesis and functionalization of monodisperse near-ultraviolet and visible excitable multifunctional Eu^{3+}, Bi^{3+}:$REVO_4$ nanophosphors for bioimaging and biosensing applications†

Alberto Escudero,*[a,b] Carolina Carrillo-Carrión,[a,c] Mikhail V. Zyuzin,[a] Sumaira Ashraf,[a] Raimo Hartmann,[a] Nuria O. Núñez,[b] Manuel Ocaña[b] and Wolfgang J. Parak[a]

Received 25th April 2016,
Accepted 9th May 2016

DOI: 10.1039/c6nr03369e

www.rsc.org/nanoscale

Near-ultraviolet and visible excitable Eu- and Bi-doped NPs based on rare earth vanadates ($REVO_4$, RE = Y, Gd) have been synthesized by a facile route from appropriate RE precursors, europium and bismuth nitrate, and sodium orthovanadate, by homogeneous precipitation in an ethylene glycol/water mixture at 120 °C. The NPs can be functionalized either by a one-pot synthesis with polyacrylic acid (PAA) or by a Layer-by-Layer approach with poly(allylamine hydrochloride) (PAH) and PAA. In the first case, the particle size can also be tuned by adjusting the amount of PAA. The Eu- Bi-doped $REVO_4$ based nanophosphors show the typical red luminescence of Eu(III), which can be excited through an energy transfer process from the vanadate anions, resulting in a much higher luminescence intensity in comparison to the direct excitation of the europium cations. The incorporation of Bi into the $REVO_4$ structure shifts the original absorption band of the vanadate anions towards longer wavelengths, giving rise to nanophosphors with an excitation maximum at 342 nm, which can also be excited in the visible range. The suitability of such nanophosphors for bioimaging and biosensing applications, as well as their colloidal stability in different buffer media of biological interest, their cytotoxicity, their degradability at low pH, and their uptake by HeLa cells have been evaluated. Their suitability for bioimaging and biosensing applications is also demonstrated.

1. Introduction

Nanoparticles (NPs) are currently attracting wide research interest due to their potential use in medical[1] or energy-conversion/storage applications. In the case of biomedically motivated research, luminescent NPs are interesting because of their optical properties, and can be used as optical biolabels for imaging of tissues or intracellular structures, as sensors to detect biological molecules, and as tracking devices.[2–7]

For biomedical applications usually uniform NPs with controlled size, shape, composition, surface chemistry and other physicochemical properties are desired,[8] given the strong effect that the morphology, size, and structure of the particles may have on many physicochemical properties of these materials.[9–12]

Among the different luminescent nanomaterials available in the literature,[13] including quantum dots[14] and nanostructures functionalized with organic dyes,[6] Rare Earth (RE) based nanophosphors exhibit important advantages due to their lower toxicity, photostability, high thermal and chemical stabilities, high luminescence quantum yields, and sharp emission bands.[15–17] These nanomaterials usually consist of an inorganic host matrix doped with luminescent lanthanide (Ln) cations. Red-emitting Eu^{3+} is frequently used as a luminescent cation, as the autofluorescence of tissues is minimized in this wavelength range.[18] The main disadvantage of Ln-doped nanophosphors is their relatively low global intensity luminescence, caused by the low absorptions of the parity forbidden Ln^{3+} 4f–4f transitions, and constituting a serious limitation for their use for imaging applications. Different energy transfers schemes from the host materials to the Ln^{3+} cations are employed to enhance the global luminescence of lanthanide-doped nanophosphors, including the use of vanadate or

---

[a] AG Biophotonik, Fachbereich Physik, Philipps-Universität Marburg, Renthof 7. D-35037, Marburg, Germany
[b] Instituto de Ciencia de Materiales de Sevilla, CSIC – Universidad de Sevilla. C. Américo Vespucio 49. E-41092, Seville, Spain. E-mail: alberto.escudero@csic.es
[c] CIC biomaGUNE. Paseo Miramón 182. E-20009, San Sebastian, Spain

† Electronic supplementary information (ESI) available: Additional details of experiments and results (NP characterization, NPs' uptake and imaging). See DOI: 10.1039/c6nr03369e

oxyfluoride matrices.[19–23] However, ultraviolet excitation radiations with wavelengths below 300 nm are normally required, resulting in limitations for the use of such materials for bioimaging. It has been reported that the Eu^{3+}:$REVO_4$ excitation peak can be shifted toward longer wavelengths upon doping with Bi^{3+}, resulting in phosphors excitable by near-ultraviolet light.[24–29]

Eu^{3+}:Bi^{3+} doped YVO_4 micro- and NPs of different morphologies (sphere-, granular-, and rod-like) have been synthesized by various wet-chemical processes including coprecipitation,[30] and hydrothermal[31–33] methods, and thin films have been produced by sol–gel processes.[34] Micrometric Eu^{3+}:Bi^{3+}:$GdVO_4$ particles have been produced by a hydrolysed colloid reaction (HCR) technique[35] and by a combustion process.[36] Gd bearing NPs are also of special interest due to their use as a relaxation agent in magnetic resonance imaging (MRI), owing to the magnetic moment and nanosecond time scale electronic relaxation time of Gd^{3+}.[37]

A functionalization process is normally required for the biomedical use of NPs. This process not only increases the colloidal stability of the NPs by introducing electrostatic and/or steric repulsions,[38] but also provides anchors for adding functional ligands of biomedical interest such as antibodies, peptides, proteins, and some anticancer drugs.[39] Functionalization of Eu^{3+}:Bi^{3+}:YVO_4 nanophosphors with additives such as sodium citrate[40] and branched polyethylenimine (BPEI)[32,33] have been reported.

Alternatively, NPs can also be coated with polymers.[41] Poly(acrylic acid) (PAA) is a frequently used polymeric ligand for the biofunctionalization of NPs, because of its negligible toxicity,[42] its hydrophilic character,[43] and its high affinity for cellular membranes.[44] Usually, the PAA surface modification of the NPs is carried out through the adsorption or ionic interaction process.[41] Another common functionalization strategy consists of the encapsulation of the NPs by multiple layers of polymers, leading to hybrid core/(polymer-)shell NPs.[45] The Layer-by-Layer (LbL) approach, which is based on the electrostatic deposition of layers of polyelectrolytes with alternating charge on the surface of the particles,[46] has been widely used to functionalize different kinds of nanostructured materials, such as gold NPs[47] and, especially, for the synthesis of polyelectrolyte capsules.[48] The application for RE-based NPs is however not common so far.[41,49]

We report here a facile and fast synthesis method of Eu^{3+}:Bi^{3+}:$REVO_4$ (RE = Y and Gd) nanophosphors, based on a homogeneous precipitation process from solutions of appropriate RE and orthovanadate precursors in ethylene glycol (EG)/water mixtures at 120 °C. Both kinds of nanophosphors are functionalized with poly(acrylic acid) (PAA) by a one-pot synthesis strategy (*i.e.* PAA is added during the synthesis process), and also by a Layer-by-Layer approach with poly(allylamine hydrochloride) (PAH) and PAA. The effect of the level of Bi^{3+} doping on the luminescence properties of both kinds of nanophosphors has also been studied, as well as their colloidal stability in different physiological buffers, their degradability at low pH, and their cell viability. Finally, we show how the europium and bismuth doped rare earth orthovanadate NPs can be used to image human cervical carcinoma (HeLa) cells by using near-ultraviolet and visible radiation as excitation sources, and as pH sensors, after their conjugation with a pH-sensitive dye such as Nile Blue. The influence of the morphology and chemical composition of the NPs on the cellular uptake is also shown.

2. Results and discussion

2.1 Synthesis, PAA functionalization and physicochemical characterization of the NPs

A homogeneous process with constant reaction kinetics is normally required to obtain uniform NPs by precipitation. This can be achieved by a slow and controlled release of the precipitating anions or cations within the solution.[50] In our case, a homogeneous precipitation is produced by using $Y(acac)_3$ as the yttrium precursor for the synthesis of YVO_4-based particles. This compound decomposes on heating, and gives rise to a slow release of the Y cations.[51] It has also been described that the presence of additives during the synthesis process, such as PAA, can affect the final morphology of the particles.[52] Moreover, a specific reaction kinetics is also demanded, which is established after an analysis of the effects of the experimental reaction parameters on the morphological features of the precipitated particles.[50] The synthesis protocol herein reported for the synthesis of europium and bismuth doped YVO_4 produces NPs with similar morphological characteristics, irrespective of the Bi content. A representative transmission electron microscopy (TEM) micrograph of the Bi20YPAA2 sample (see Table 1 for sample information) is shown in Fig. 1A. As it can be observed, NPs with a quasi-spherical morphology and a mean size of 93 nm ± 7 nm were obtained. The NPs are single crystals, as shown by the SAED pattern obtained from a single particle, which is compatible with the tetragonal symmetry of YVO_4 (space group $I4_1/amd$) and could be indexed along the [001] zone axis (inset in Fig. 1A). The high-angle annular dark-field (HAADF) image of the sample Bi20YPAA2 indicates a homogeneous distribution of bismuth in the NPs (Fig. 1D). The mean hydrodynamic diameter of such nanoparticles obtained by dynamic light scattering (DLS) was 108 ± 10 nm, which is expected for well-dispersed particles free of aggregation. The analogous sample synthesized in the absence of PAA (sample Bi20Y) consisted of NPs with slightly sharper edges and a mean size of (107 ± 14) nm (Fig. S1A†). Also in this case, the mean hydrodynamic diameter of the Bi20Y NPs obtained by DLS (138 ± 7 nm) indicated that they were free of aggregation. It should be noted that the presence of bismuth in the europium-doped YVO_4 NPs had almost no effect on the particle morphology, since similar NPs with a mean size of 88 ± 14 nm were observed in the absence of Bi (sample Bi0YPAA2, Fig. S1B†). By increasing the concentration of PAA from 2 to 8 mg mL^{-1} (sample Bi20YPAA8), a significant decrease in the mean particle size to 51 ± 5 nm was observed (Table 2) without alteration of the morphology (Fig. 1B). This difference in the particle size produced

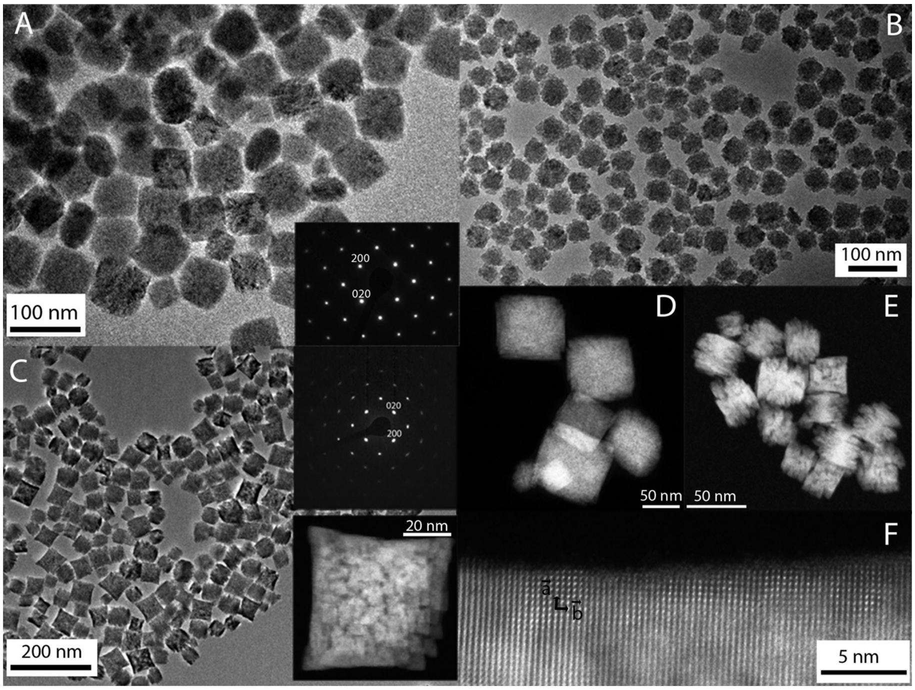

Fig. 1 TEM micrographs of the Bi20YPAA2 (A, scale bar 100 nm), Bi20YPAA8 (B, scale bar 100 nm), and Bi20GdPAA (C, scale bar 200 nm) samples. HAADF images of the Bi20YPAA2 (D, scale bar 50 nm), and Bi20GdPAA (E, scale bar 50 nm) samples. (F, scale bar 5 nm) HRTEM image of a particle of the Bi20GdPAA2 sample.

on the addition of PAA to the solutions containing the precursors may be attributed to the adsorption of these molecules on the NP surface, which could block the growth of the NPs.

Similar results were observed for the Eu- Bi-doped $GdVO_4$ samples. A representative TEM micrograph of the Bi20GdPAA sample is shown in Fig. 1C. As it can be seen, non-aggregated NPs with a smaller size and slightly sharper edges when compared with those based on YVO_4 (TEM size 40 ± 8 nm, DLS 41 ± 2 nm) were produced after the synthesis in the presence of PAA. Such NPs were also single crystals, as inferred from the SAED pattern of a single particle, which is compatible with tetragonal $GdVO_4$ (space group $I4_1/amd$), zone axis [001], and from the high resolution TEM images (insets of Fig. 1C and F). Analogous to the yttrium vanadate samples, a homogeneous distribution of Bi in the NPs was indicated by the HAADF-TEM images (Fig. 1E). Much more polydisperse and bigger NPs with a not so well defined shape (TEM size 51 ± 15 nm, DLS 58 ± 4 nm, Fig. S1C†) were obtained in the absence of PAA (sample Bi0Gd). Similar to the YVO_4-based NPs, the presence of Bi did not affect the particle morphology, since NPs with a mean size of 39 ± 7 nm were obtained in the absence of Bi (sample Bi0GdPAA, Fig. S1D†). A summary of the data corresponding to all the synthesized samples is shown in Table S2.†

The presence of PAA on the surface of both Bi20YPAA2 and Bi20GdPAA NPs was confirmed by Fourier transform infrared spectroscopy (FTIR) analysis. The FTIR spectra of the Bi20Y, Bi20Gd, Bi20YPAA2, and Bi20GdPAA samples are shown in Fig. 2. In all the samples, the characteristic bands of vanadate anions (<1000 cm^{-1})[53] and adsorbed water (broad bands at

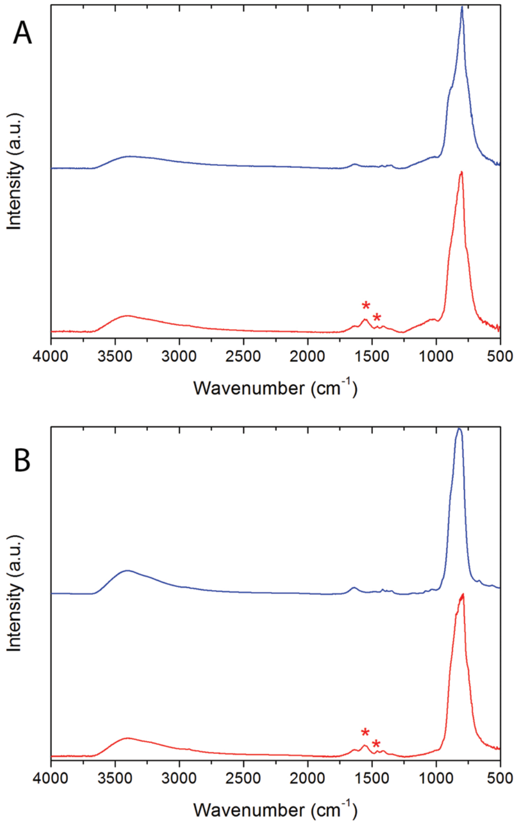

Fig. 2 Fourier transform infrared spectroscopy (FTIR) spectra of (A) the Bi20Y (blue) and Bi20YPAA2 (red) samples; and (B) of the Bi20Gd (blue) and Bi20GdPAA (red) samples.

3400 and 1600 cm^{-1}) can be observed, as well as some much weaker features in the 1500–1300 cm^{-1} region, which can be attributed to the presence of carbonate anions from the adsorption of atmospheric CO_2.[54] Samples Bi20YPAA2 and Bi20GdPAA show extra signals around 1458 and 1550 cm^{-1} (marked with asterisks in Fig. 2), which can be ascribed to the symmetric and antisymmetric stretching frequencies of the carboxylate ion (COO^-), respectively.[52] Taking into account that the carbonyl stretching (C=O) vibration appears at 1717 cm^{-1} for pure PAA, the shift towards lower frequencies indicates that most of the carboxylate functional groups of the polymer are fully ionized[55] and, therefore, that the PAA molecules are bonded to the NP surface though the carboxylate groups.

Further evidence of the PAA functionalization of the particles was obtained by comparing the ζ-potential of aqueous suspensions of the non-functionalized and PAA-functionalized particles. Bi20Y particles showed a ζ-potential of −19 mV in water at pH 7, whereas the value of this magnitude for the NPs synthesized in the presence of PAA was −42 mV at the same pH. Analogously, the ζ-potential of the Bi20GdPAA NPs was −41 mV, to be compared to the one of −25 mV as observed for the non-functionalized Bi20Gd particles. Thus, NPs synthesized in the presence of PAA are already functionalized with carbonyl groups. An estimation of the amount of PAA on the surface of the PAA-functionalized NPs was obtained from thermogravimetry (TG) analysis (Fig. S2†). The weight loss observed at temperatures below 250 °C can be associated with the elimination of absorbed water. At higher temperatures (up to 600 °C), the loss most likely is connected with the decomposition of the adsorbed PAA molecules, which was higher for the sample prepared with more PAA (*ca.* 2% for sample Bi20YPAA2, *ca.* 15% for sample Bi20YPAA8 – including more adsorbed water-, and *ca.* 4% for sample Bi20GdPAA).

The successful incorporation of europium and bismuth into the NPs was evidenced from the energy dispersive X-ray spectra (EDX) obtained for single particles, which displayed europium and bismuth peaks, in addition to those of yttrium, vanadium, gadolinium and oxygen (Fig. S3†). Moreover, no extra particles with different morphologies or with a higher Bi or Eu content were observed. Induced coupled plasma atomic emission spectroscopy (ICP-AEP) measurements indicated that the experimental molar ratios corresponding to the doped particles were in good agreement with the nominal values (Table S3†).

The X-ray diffraction (XRD) diagrams obtained for the Bi0YPAA2 and Bi20YPAA2 samples (Fig. 3A) consisted of peaks that are very similar to the standard pattern of tetragonal YVO_4 (PDF 01-070-1281). Similar results were observed for the Bi0GdPAA and Bi20GdPAA samples, whose XRD diagrams (Fig. 3B) were also very similar to the standard pattern of tetragonal $GdVO_4$ (PDF 01-086-0996). Based on these data, the possible formation of slightly non-stoichiometric phases of rare earth orthovanadates can however not be fully discarded.[56] It should also be pointed that for similar orthovanadate systems, an excess of [Na_3VO_4] in the starting solutions was used to adjust the precipitation kinetic, yielding NPs with smaller size.[19,21,23] The slight differences in peak positions and intensities in both Y and Gd bearing samples when increasing the Bi content (see peaks under the vertical guide lines) indicate changes in the unit cell dimensions and composition. This was confirmed by the measurements of the unit cell parameters of all the doped samples synthesized in the presence of PAA, which showed in both cases a linear increase of the unit cell volume as the Bi doping level increased (Table 2, Fig. S4†). Such results are in agreement with the higher ionic radius of the Bi^{3+} cations (1.17 Å) when compared to those of Y^{3+} (1.019 Å) and Gd^{3+} (1.053 Å), all of them in eightfold coordination.[57] The average crystal size (Table 2) estimated by using the Scherrer formula from several XRD peaks (101, 200, 112, 220, and 321) for all the particles was very similar to the size observed by TEM and DLS, also suggesting that the particles were single crystals.

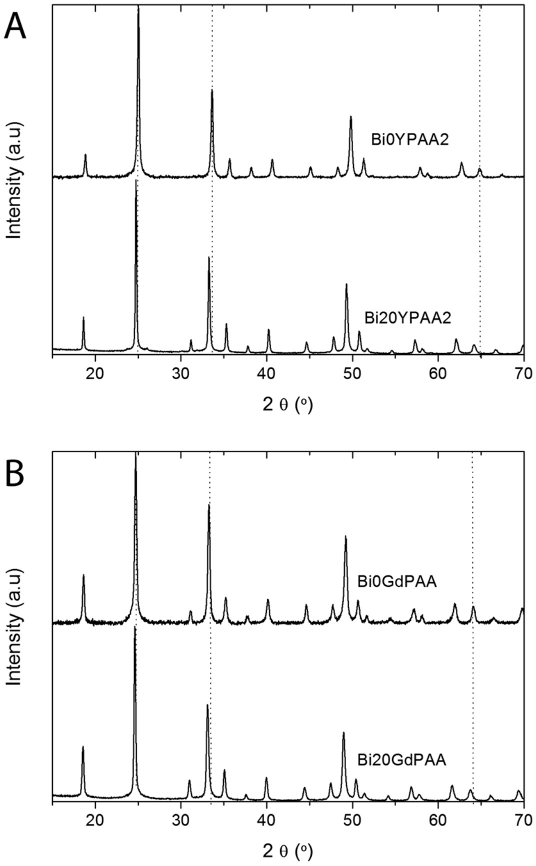

Fig. 3 XRD diagrams of (A) the Bi0YPAA2 and Bi20YPAA2 samples; and (B) of the Bi0GdPAA and Bi20GdPAA samples. Vertical guides are only intended as a guide to the eye.

2.2 Layer-by-Layer functionalization

The LbL functionalization of NPs usually requires an optimization of the experimental parameters in order to avoid particle agglomeration. Several variables are known to play an important role in this process, including the polyelectrolyte stoichiometric excess, the NP concentration, the size and degree of polymerization of the polyelectrolyte chains, and the salt concentration.[58] In general terms, an excess of polyelectrolyte, low NP concentrations, and short polyelectrolyte chains help obtain NPs free of aggregation. Regarding the salt concentration, low concentrations prevent agglomeration, but high concentrations normally increase the polyelectrolyte amount that is deposited onto the NP surface.[59]

Functionalized particles free of aggregation (as concluded from the fact that hydrodynamic diameters as determined by DLS were only slightly bigger than inorganic core diameters as determined by TEM) were obtained for both kinds of bare NPs (samples Bi20Y and Bi20Gd) by using 10 mg per mL polyelectrolyte solutions in 0.05 M NaCl aqueous solutions at pH 6.5, as described in the Experimental section. The success of functionalization and the absence of a significant particle agglomeration were confirmed by the surface charge reversal observed after the deposition of every polyelectrolyte layer, and by the evolution of the hydrodynamic diameter of the particles, respectively (Fig. 4). The selection of PAH and PAA as polymers for the Layer-by-Layer functionalization of the NPs also provides reactive –COOH and $-NH_2$ groups, and increases the possibility of further conjugation with different molecules of biomedical interest.

2.3 Colloidal stability

The colloidal stability of both, PAA- and LbL PAH/PAA/PAH functionalized NPs, was analyzed by studying the mean hydrodynamic diameter (d_h) obtained by DLS in water and in different buffer media of biological interest, containing salt and proteins.[60] The evolution of the hydrodynamic diameter with increasing time was also studied.

The hydrodynamic diameters measured for freshly prepared suspensions of PAA-functionalized NPs in different buffers are shown in Fig. 5A and B, and in Table S4.† For both PAA-functionalized NPs similar hydrodynamic diameters were observed in water at pH 7 and in MES buffer at pH 6.5. Such values are very close to the size determined by TEM for both samples, indicating the absence of significant aggregation and, therefore, colloidal stability in both media. Bi20YPAA2 NPs also showed colloidal stability in PBS buffer at pH 7.4, whereas some aggregation was observed for the Bi20GdPAA NPs in this same buffer. A strong level of aggregation was observed for both PAA-functionalized NPs in cell medium, which was minimized in serum-supplemented cell medium. Proteins in solution are well-known to attach to the surface of the NPs, forming the so-called protein corona,[61] and provide the NPs with additional colloidal stability. No changes were observed in the mean hydrodynamic diameter of the YVO_4-based PAA-functionalized NPs (sample Bi20YPAA2) with increasing aging time in water at pH 7, MES buffer at pH 6.5, PBS at pH 7.4, and serum-supplemented cell medium (Fig. S5A–D†), and similar results were observed for the Bi20GdPAA sample with increasing aging time in water at pH 7, in MES at pH 6.5, and serum-containing cell medium, with only some aggregation when aging in PBS at pH 7.4 (Fig. S5F–J†), manifesting that no particle aggregation took place upon aging in these buffer media at the studied pHs.

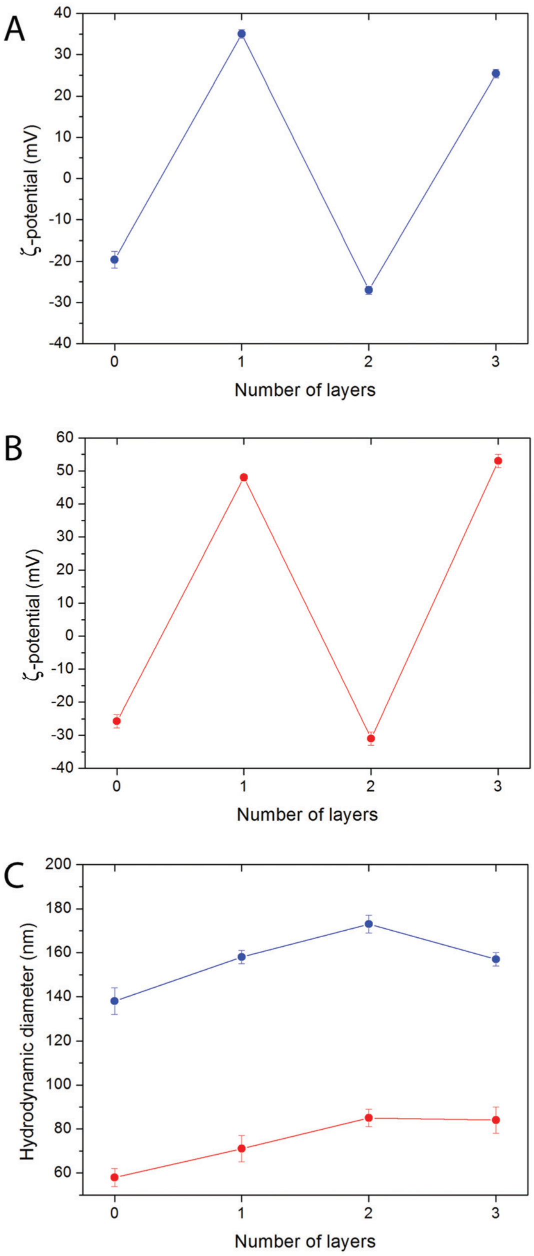

Fig. 4 ζ-Potential of the Bi20Y (A) and Bi20Gd (B) nanoparticles functionalized with PAH and PAA by the LbL technique after the deposition of different polyelectrolyte layers, measured in water at pH 7. (C) Evolution of the hydrodynamic diameter of the Bi20Y (blue) and Bi20Gd (red) functionalized nanoparticles with the number of deposited polyelectrolyte layers.

Data corresponding to the PAH/PAA/PAH LbL functionalized YVO_4 NPs are shown in Fig. 5C and Table S3.† No significant aggregation was observed in MES buffer at pH 6.5. It should be mentioned that at least two polyelectrolyte layers were required to achieve colloidal stability in MES buffer at pH 6.5 (Fig. S6†). A decrease of the colloidal stability was observed for the LbL functionalized particles in both PBS at pH 7.4 and

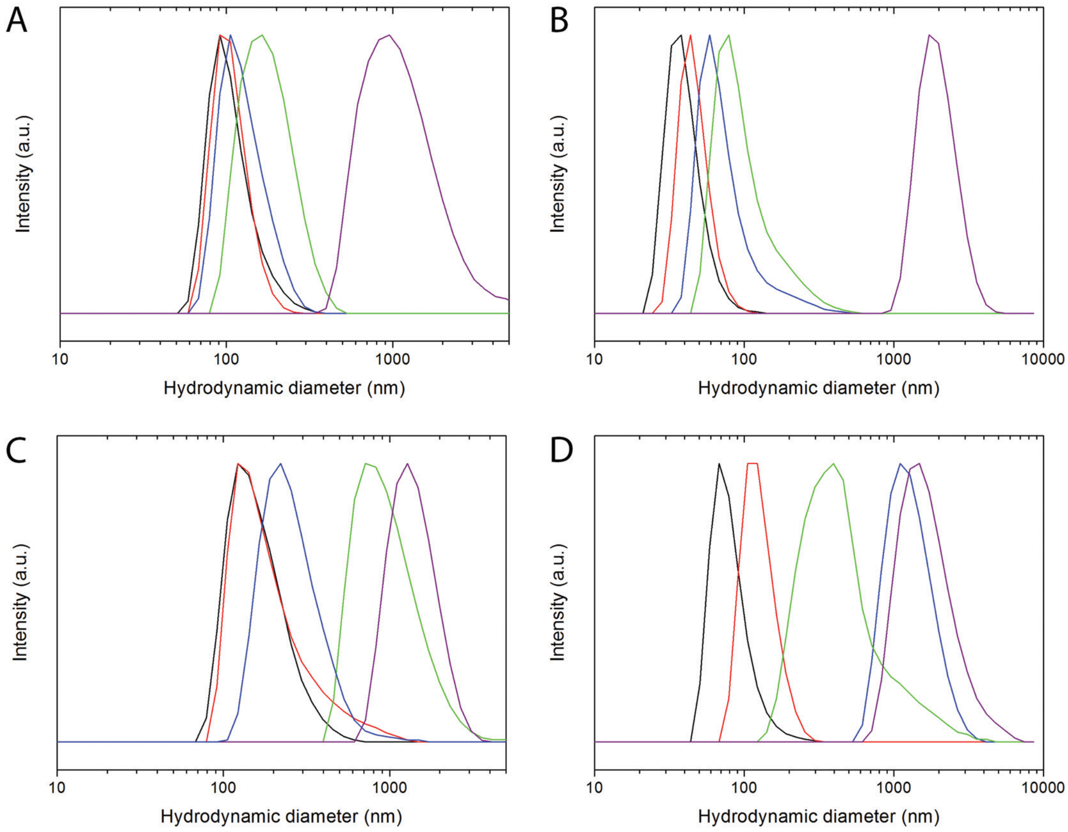

Fig. 5 Hydrodynamic diameter of the Bi20YPAA2 (A), Bi20GdPAA (B), Bi20Y@PAH@PAA@PAH LbL-functionalized (C), and Bi20Gd@PAH@PAA@PAH LbL-functionalized (D) nanoparticles in water at pH 7 (black lines), MES 50 mM at pH 6.5 (red lines), PBS at pH 7.4 (blue lines), serum-supplemented cell medium (green lines), and cell medium (purple lines).

in cell medium. Similar to the observation for the PAA-functionalized NPs, a considerable reduction in the agglomeration level was observed for the LbL functionalized particles in serum-supplemented cell medium, which was however not so strong as in the previous example. At this point, it worth pointing out that a similar level of aggregation (d_h = 240 nm, Fig. S7A†) was observed for the non-functionalized bare particles (sample Bi20Y) in serum-supplemented cell medium, which indicates the strong effect of the protein absorption on the final colloidal stability of the NPs. Slightly worse colloidal stability was observed for the LbL functionalized $GdVO_4$-based NPs (Fig. 5D, Table S4†). Very slight agglomeration was also observed for the bare Bi20Gd NPs in serum-supplemented cell medium (Fig. S7B†). The level of aggregation of both kinds of LbL functionalized NPs increased with aging in MES, PBS, and cell medium. No changes were observed with aging time in water at pH 7 and in serum-supplemented cell medium (Fig. S5†).

These results indicate that the colloidal stability of the one pot PAA synthesized and functionalized NPs is higher than the one shown by the NPs functionalized in a second step by the LbL approach. The incorporation of either functionalizing agents or adsorbed organic molecules onto the NP surface during the synthesis process seems to play a role in the final colloidal stability of the particles, at least when dealing with polymeric functionalizing agents. In particular, incorporation of multiple particles into one polymer shell may lead to aggregation. However, the LbL strategy offers a useful functionalization alternative for systems in which no functionalizing agents attach to the NP surface during the synthesis process. The colloidal stability of the NPs functionalized by the LbL strategy increases with the number of deposited layers.

2.4 Optical properties

Excitation spectra of both, 8% Eu- 20% Bi-doped YVO_4 and $GdVO_4$ PAA functionalized NPs (samples Bi20YPAA2 and Bi20GdPAA, Fig. 6A and B, respectively) were recorded by monitoring at a wavelength of 622 nm, which corresponds to the main emission line of Eu^{3+} cations in rare earth vanadate matrices. Both spectra show a broad band with maxima at 342 nm, associated with the indirect excitation of the Eu^{3+} cations. For both, Y- and Gd-bearing nanophosphors (*i.e.* Bi-free samples), a broad excitation band with a maximum centered at around 280 nm can be observed (Fig. S8†).[19,21] This band has been ascribed to the optical excitation of the vanadate anions (originated from the $O^{2-} \rightarrow V^{5+}$ charge transfer within the vanadate groups), followed by an energy transfer to the Eu^{3+} cations.[62] The incorporation of Bi into the $REVO_4$

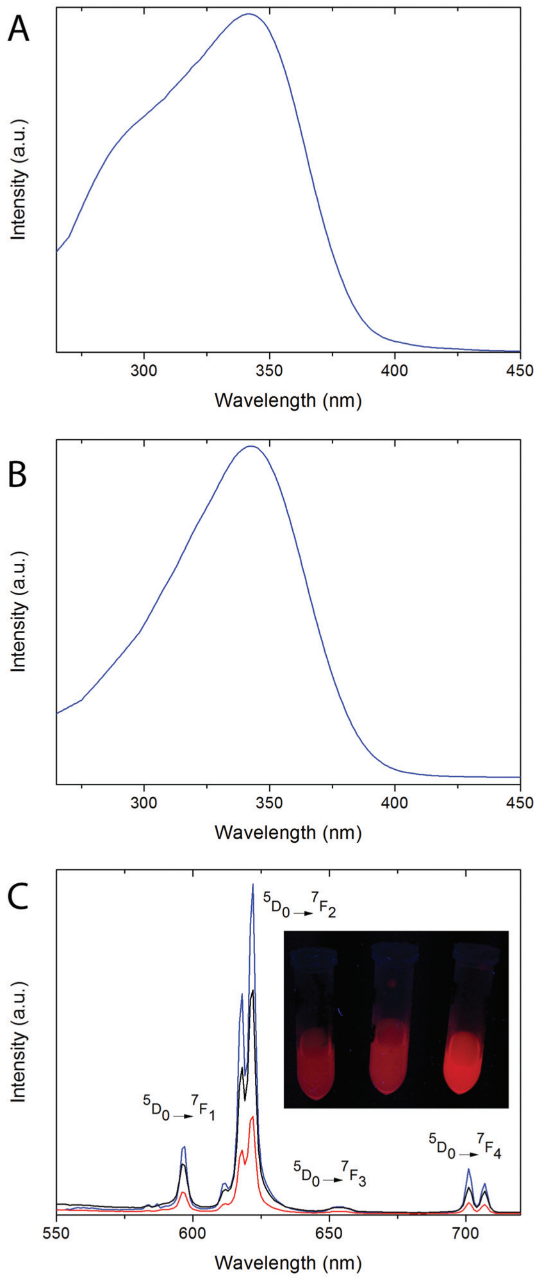

Fig. 6 Excitation spectra (emission recorded at λ_{em} = 622 nm) of the Bi20YPAA2 (A) and Bi20GdPAA (B) samples. (C) Emission spectra of the Bi20GdPAA (blue line), Bi20YPAA2 (black line), and Bi20YPAA8 (red line) samples (excitation at λ_{exc} = 342 nm). The photograph shows the red luminescence of water suspensions (0.05 mg mL^{-1}) of the Bi20YPAA8 (left), Bi20YPAA2 (center), and Bi20GdPAA (right) samples when irradiated with a UV lamp.

lattices produces changes in both the shape and the position of the maximum of the broad absorption band. Increasing the Bi content produces wider absorption bands with the maxima shifting toward longer wavelengths. (Fig. S8†). The observed changes can be explained by the appearance of an extra charge transfer band from the 6s level of Bi^{3+} to the 3d levels of V^{5+}, which is centered around 340 nm.[24]

Fig. 6C shows the emission spectra of the suspensions of the Bi20YPAA2 (black line), Bi20YPAA8 (red line), and Bi20GdPAA (blue line) samples, recorded under a UV excitation of 342 nm. The spectra display the typical emissions corresponding to the $^5D_0 \rightarrow {}^7F_J$ (J = 1, 2, 3, and 4) electronic transitions expected for the Eu^{3+} cation.[62] The most intense emission ($^5D_0 \rightarrow {}^7F_2$ transitions) is split into two bands at 618 and 622 nm owing to the crystal field.[62] It can also be observed that the relative intensity of the $^5D_0 \rightarrow {}^7F_2$ emission band is in all cases higher than that associated with the $^5D_0 \rightarrow {}^7F_1$ transition, which is expected for Eu^{3+} cations located in crystallographic sites without an inversion center. This is compatible with Eu^{3+} cations replacing Y^{3+} or Gd^{3+} on the normal yttrium sites of the tetragonal REVO$_4$ structure, in which the RE sites show a local symmetry of D_{2d}.[62]

The different emission intensities observed for the different samples should be connected with their different luminescence quantum yields, since the spectra were recorded from NP suspensions owing to the same NP concentration. At least qualitatively, the GdVO$_4$ host material seems to show a higher luminescence quantum yield than YVO$_4$. The differences observed for the YVO$_4$-based NPs of different sizes show that bigger particles are more efficient. This should be connected with their lower surface area per particle volume. As the size of the NPs decreases, there is a significant increase of the surface area per particle volume, as well as an increase in the number of surface defects and higher number of capping ligand molecules, causing a decrease in the luminescence efficiency.[63,64]

It should also be mentioned that it has been reported that Eu, Bi-doped YVO$_4$ might exhibit photobleaching under continuous UV irradiation.[65,66] In our case, Bi20YPAA2 NPs were continuously irradiated with UV light (Fig. S9†). After 10 minutes of irradiation, around 80% of the initial intensity was still observed, being reduced to about 70% after 25 minutes of irradiation.

2.5 Cellular uptake and imaging

Human cervical carcinoma cell line (HeLa) cells were used as a system to show the suitability of both Eu- Bi-doped YVO$_4$ and GdVO$_4$ NPs for bioimaging. Two different microscopes were used to image the NPs. On one hand, the broad absorption band of the NPs with a maximum at around 342 nm permits their excitation with near-ultraviolet light in a fluorescence microscope. On the other hand, the shift of the absorption band of the Bi-doped vanadate matrices toward longer wavelengths makes also possible their excitation with a visible radiation by using a laser as the excitation source in a confocal laser scanning microscope (cLSM). The study of the NP internalization by the cells was performed by observing the co-localization of the fluorescence of the NPs with those produced by different endocytic fluorescent markers that specifically attach to the cell membranes and organelles.[67] A strong red luminescence in the interior of the cells could be observed after irradiation at (340 ± 24) nm after 24 h of incubation (illustrated in Fig. 7 for the Bi20YPAA2 sample). This fluorescence was clearly co-localized with the yellow one produced by

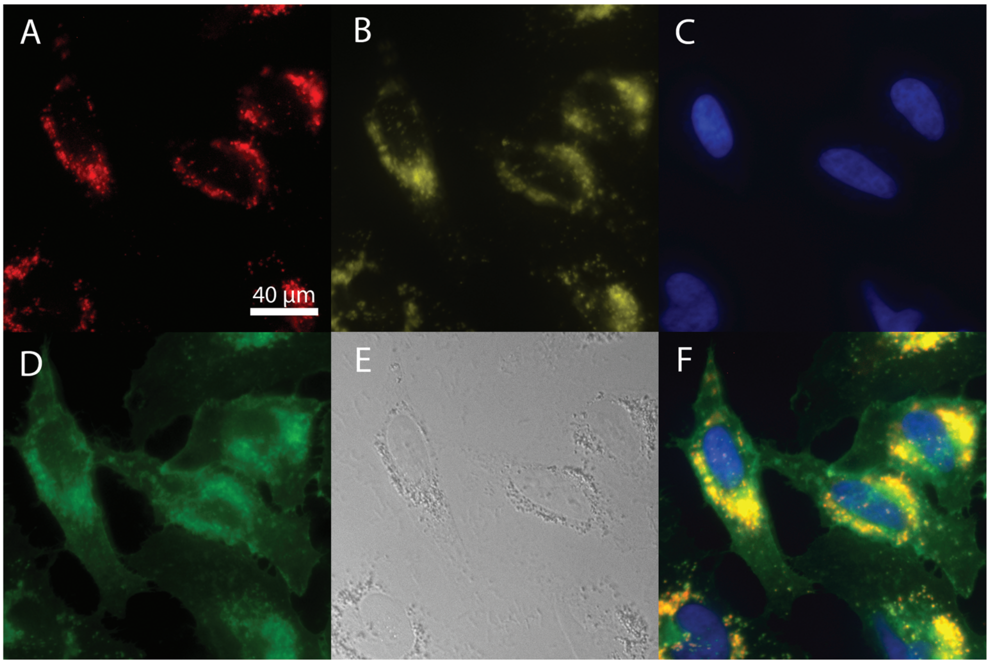

Fig. 7 Fluorescence images of HeLa cells incubated with Bi20YPAA2 nanoparticles for 24 h. (A) Red channel, nanoparticles; (B) yellow channel, lysosomes; (C) blue channel, cell nuclei; (D) green channel, cell membranes; (E) transmission image; and (F) merged all channels.

LAMP1, a marker for the membrane of lysosomes, indicating that the NPs are eventually located in the cell's lysosomes after being internalized. Such red fluorescence was not observed under UV light excitation in the control experiments, in which HeLa cells were incubated without NPs (Fig. S10†). PAA-functionalized Eu- Bi-doped $GdVO_4$ NPs, as well as both Eu- and Bi-doped YVO_4 and $GdVO_4$ NPs functionalized by LbL could also be observed in the cell interior (Fig. S11–S14†).

As it was previously mentioned, it is also possible to image both, YVO_4- and $GdVO_4$-based NPs with a confocal laser scanning microscope (cLSM) using visible light as the excitation source (wavelength of 405 nm, laser power 20%). The red luminescence of the NPs can clearly be observed to be associated with HeLa cells after 24 hours of incubation (Fig. 8, illustrated for sample Bi20YPAA2). Images of the control sample and of HeLa cells incubated with samples Bi20YPAA8 and Bi20GdPAA are shown in Fig. S15.†

2.6 Biosensing applications

The presence of free carboxyl groups on the NP surface not only provides colloidal stability but also facilitates the conjugation of the NPs with various biomolecules, which paves way for further bio-applications. In this work, Nile Blue (NB) was chosen as the fluorescent pH indicator, since it has an amino group that is capable of forming a covalent bond with the carboxyl groups of the PAA layer onto the NP surface. Samples Bi20YPAA2 and Bi20GdPAA were chosen for conjugation with Nile Blue.

Changes of the fluorescence response of the NB-PAA-NPs towards pH were evaluated over a wide pH range (pH = 3–11) recording independently the emission of the Eu^{3+} ions from the NP cores (excitation wavelength 342 nm) and the emission of the NB from the NP shells (excitation wavelength 600 nm). The maximum emission of the Eu^{3+} ions at 622 nm was found to be insensitive to the pH value and therefore can be used as reference. The emission of the NB attached to the NPs was recorded at 675 nm, and showed a clear dependence with the pH (illustrated in Fig. 9A for the Bi20YPAA2 NPs conjugated with Nile Blue at different pH values). Such behaviour allowed the use of the ratiometric intensity at these two different emission wavelengths as analytical signal, which is advantageous in terms of accuracy and reliability, because errors associated with environmental variations, probe distribution, and instrumental performance are diminished. The sigmoidal response obtained from the calibration curve of the ratio between the pH and the emission intensities at 622 and 675 nm (Fig. 9B) demonstrates that such particles can be used as pH sensors at pH between 4 and 11. A similar behaviour was observed for the $GdVO_4$ based nanophosphors (sample Bi20GdPAA) conjugated with NB (Fig. 9C).

2.7 Biocompatibility, cell viabilities and degradation of the particles

Biocompatibility studies of both, Eu- Bi-doped YVO_4- and $GdVO_4$-based nanophosphors were undertaken by evaluating the cell viability of HeLa cells on the basis of the metabolic activity of living cells using a Resazurin based assay.[68] PAA-functionalized YVO_4 based NPs (sample Bi20YPAA2, Fig. 10A) showed under the used exposure conditions negligible toxicity effects, with viability percentages around 75–80% for concen-

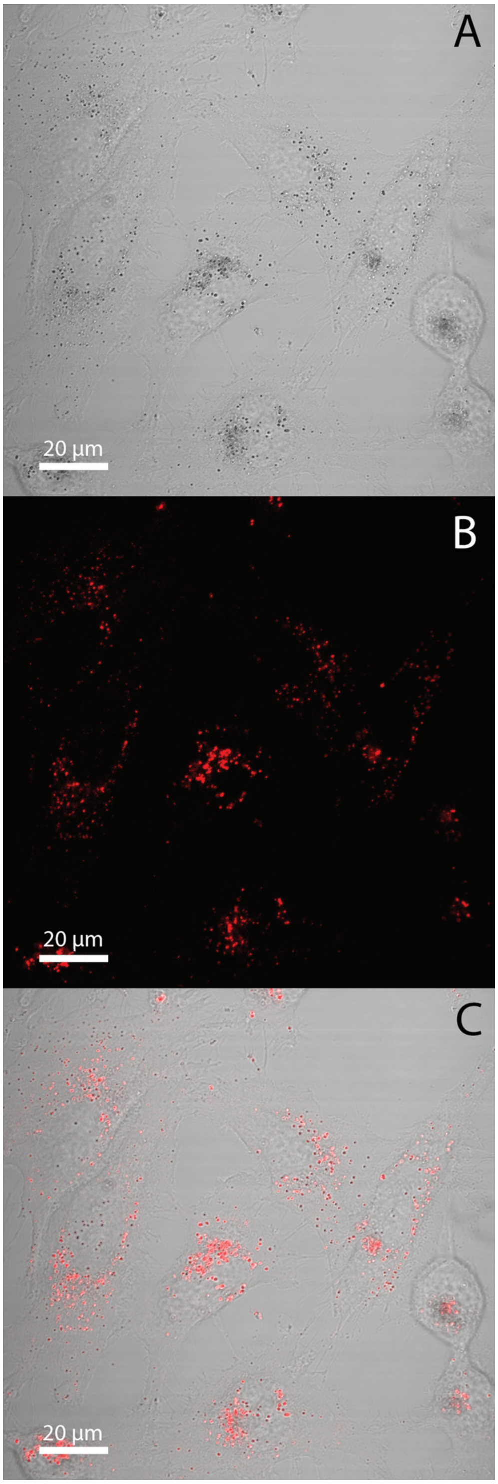

Fig. 8 Confocal microscopy images of HeLa cells incubated with Bi20YPAA2 nanoparticles for 24 hours. (A) Transmission channel, (B) fluorescence channel, (C) merged image.

trations up 1 mg mL^{-1}, and a LD$_{50}$ value measured from the sigmoidal curve (logistic dose response fit) of 1.52 ± 0.61 mg mL^{-1}. These toxicity data show low toxicity in comparison to similar particles,[33] which is probably associated with the low toxicity of the PAA.[42] However, an increase of the cytotoxicity as the particle size decreases is observed (sample Bi20YPAA8, Fig. 10A), with a measured LD$_{50}$ value of 0.16 ± 0.09 mg mL^{-1}. The PAA-functionalized GdVO$_4$ based NPs (sample Bi20GdPAA, Fig. 10B) showed much less toxic effects than their YVO$_4$-based counterparts of similar size, with a measured LD$_{50}$ value of 1.10 ± 0.29 mg mL^{-1}. Such results indicate that the incorporation of Bi into the GdVO$_4$ particles had no considerable effects on the final cytotoxicity of the NPs, since similar values have been reported for the same Bi-free particles.[21] The LbL functionalization of both kinds of nanophoshors with PAH and PAH layers reduced their cytotoxicity effects (Fig. 10A and B), as it has been observed in similar systems.[69,70] These cytotoxicity results indicate the potential suitability of such nanophosphors for sensing and cell imaging applications, even more when taken into account that the NP concentrations used in cell imaging and FACS experiments were between 1 or 2 orders of magnitude lower than the measured LD$_{50}$ values. However, it clearly needs to be stated that concerning future *in vivo* use extended toxicity studies would be required, involving, in particular, the possible effects of long-term exposure.

The dissolution of the particles at low pH was carried out under conditions mimicking the lysosome, namely acidic pH, by analysing the evolution of the hydrodynamic diameter measured by DLS with increase in the aging time in MES 50 mM buffer at pH 3.5 (Fig. 11). Both, Bi20YPAA2 and Bi20GdPAA NPs aggregate in MES buffer at pH 3.5, forming agglomerates of around 1 µm. In both cases the size of the agglomerates decreased with increase in the aging time, and finally clear solutions were observed (Fig. S16†). This shows how both, YVO$_4$- and GdVO$_4$-based NPs can be degraded in the cell lysosomes, where eventually the NPs are located, resulting in an efficient method for the NP excretion.

2.8 Flow cytometry study

To reveal the influence of both, the chemical composition and the size of the NPs on the cellular uptake, flow cytometry studies with HeLa cells were performed for samples Bi20YPAA2, Bi20YPAA8, and Bi20GdPAA. Fig. 12A shows the mean red intensity fluorescence associated with every cell with increase in the incubation time. In general terms, this value increases with increase in the incubation time for the three analysed samples, indicating that the amount of NPs internalized by HeLa cells increases with time. After 24 hours of incubation, the highest red fluorescence was observed for the Bi20YPAA2 sample (black bar), followed by Bi20GdPAA (blue bar) and Bi20YPAA8 (red bar). The 2D density plots of the control measurements are shown in Fig. S17.† Such results, which are indeed consistent with the LSM images taken for HeLa cells after NP incubation (Fig. 8 and Fig. S14,† at least qualitatively), should however not be related to the amount of NPs associated with the cells, since the emission of the analyzed samples upon excitation at 355 nm depends on both chemical composition and the NP size (Fig. S10†). These different emission intensities were taken into account in Fig. 12B, whose results can then be related to the amount of

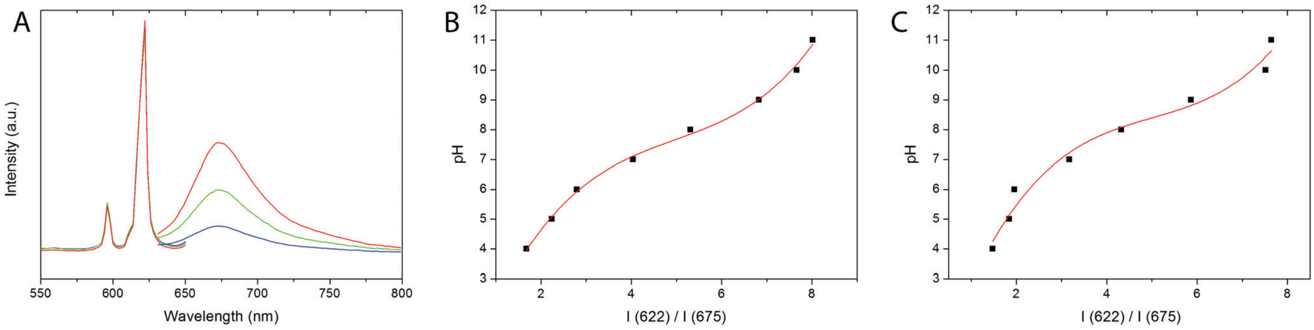

Fig. 9 (A) Emission spectra of the Bi20YPAA2 nanoparticles functionalized with Nile Blue (NB) at pH 5 (red), 7 (green), and 10 (blue). Emission of Eu^{3+} (left part) was collected with excitation at $\lambda_{ex} = 342$ nm, while λ_{ex} for NB was 600 nm (emission on the right part). (B) Intensity ratio of the Eu^{3+} ($\lambda_{em} = 622$ nm, $\lambda_{ex} = 342$ nm) and the NB ($\lambda_{em} = 675$ nm, $\lambda_{ex} = 600$ nm) emission at different pH values for the Bi20YPAA2-NB nanoparticles, and Bi20GdPAA-NB particles (C). In both last cases, the error bars are smaller than the size of the symbols.

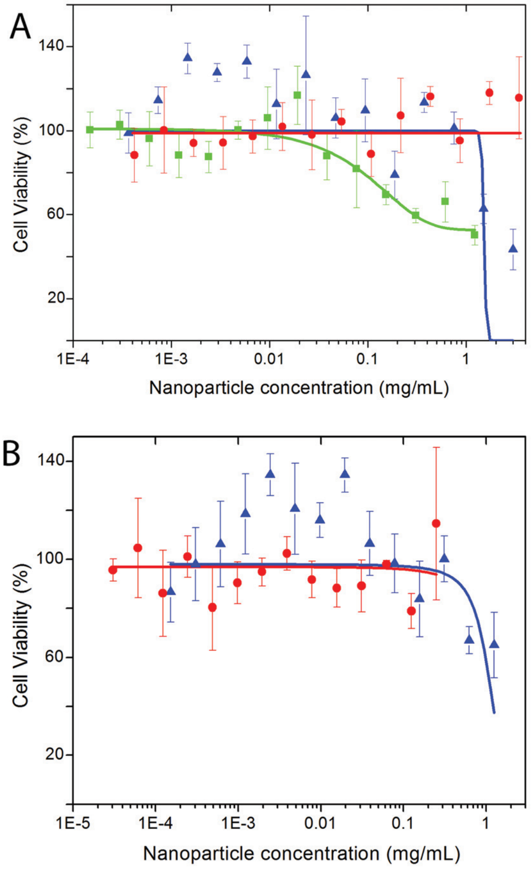

Fig. 10 Cell viabilities for HeLa cells observed after 24 hours of incubation of (A) YVO_4-based nanoparticles (Bi20YPAA2, blue triangles; Bi20YPAA8, green cubes; and Bi20Y sample LbL-functionalized with PAH and PAA, red circles); and (B) $GdVO_4$-based nanoparticles (Bi20GdPAA, blue triangles; and Bi20Gd sample LbL functionalized with PAH and PAA, red circles). 100% viability corresponds to control cells which have not been exposed to NPs. The sigmoidal curves for the fits are also shown.

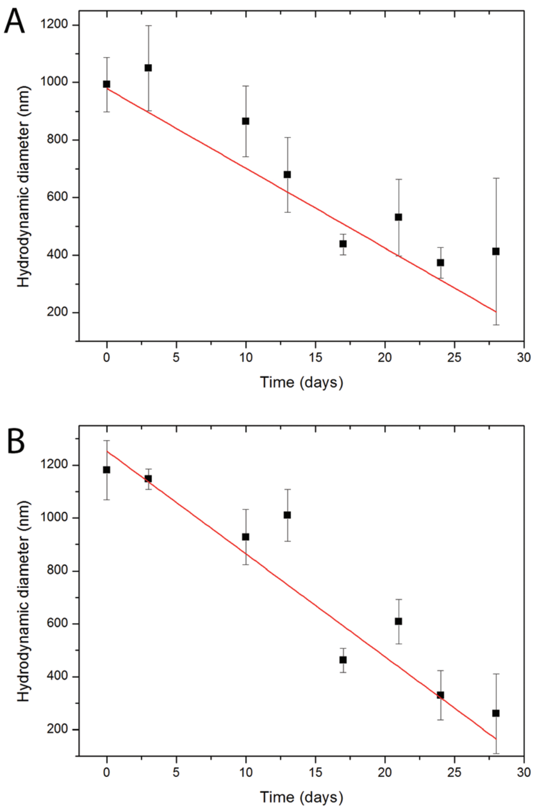

Fig. 11 Evolution of the hydrodynamic diameter of Bi20YPAA2 (A) and Bi20GdPAA (B) NPs in MES 50 mM buffer at pH 3.5 at room temperature after different incubation times The lines represent a guide to the eye.

NPs associated with the HeLa cells. A much higher amount of YVO_4-based NPs is associated with HeLa cells at any time, when compared to $GdVO_4$-based NPs. This is clearly observed when comparing the uptake of NPs of similar sizes but of different compositions, since the amount of particles of the Bi20YPAA8 sample associated with HeLa cells after 24 h of incubation is about 5 times higher than the observed for Bi20GdPAA NPs. Uptake of most NPs by cells takes place *via* endocytosis, whereby alterations in the characteristics of nanomaterials such as the radius of curvature, surface functionalization, size, geometry, NP volume, charge, and toxicity can drastically affect the uptake mechanisms of the NPs.[60,71–73,74]

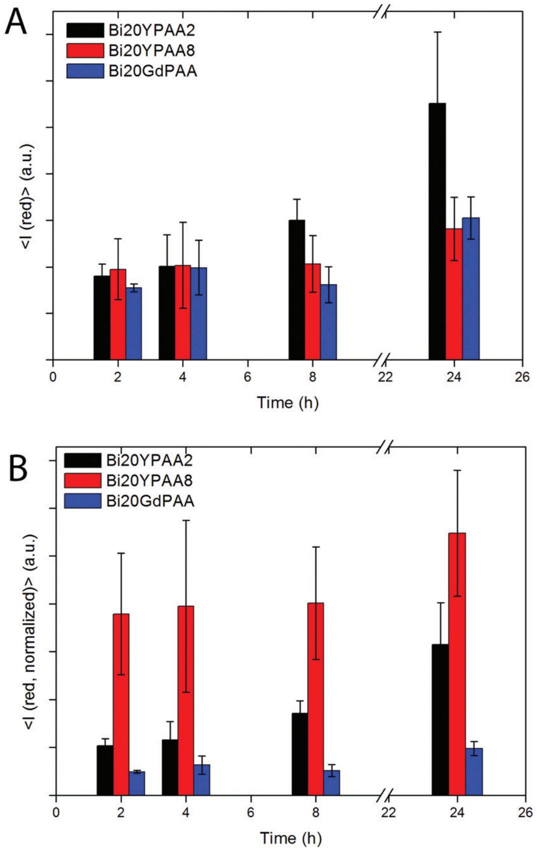

Fig. 12 (A) Average red intensity emission associated with every cell after different incubation times as obtained by flow cytometry. (B) The normalized values are taking into account the different emission intensities of the analyzed samples.

The possible effect of the slightly different morphology shown by the $GdVO_4$-based NPs, which consisted of particles with slightly sharper edges (Fig. 1C), should however not be ignored. The fact that particles with higher aspect ratios (*i.e.* rods) are normally taken up faster than spherical particles[75,76] may have some effect on the NP uptake, as reported here. Moreover, there is also indication that there is an optimum NP size yielding the fastest NP uptake.[76] In this study, 51 nm YVO_4-based particles (sample Bi20YPAA8) were up taken 2–3 times faster than the bigger 93 nm particles (sample Bi20YPAA2). Such results also suggest the existence of a correlation between the observed cytotoxicity and the amount of NP internalized by the cells, as the toxicity of the particles increases with the amount of up taken NPs of the same chemical composition.

3. Conclusions

Monodisperse near-ultraviolet and visible excitable NPs with a quasi-spherical morphology based on YVO_4 and $GdVO_4$ have been produced after doping with europium and bismuth by precipitation at 120 °C in a mixture of ethylene glycol and water (70 : 30 by volume) and appropriate rare earth precursors. The particle size could be tuned by modifying the amount of added PAA. The NPs can efficiently be excited in the near-ultraviolet and visible range, with an excitation maximum up to 342 nm, and emit the characteristic red light of europium(III), whose intensity is higher for the $GdVO_4$-based NPs than for the YVO_4-based ones. PAA-functionalized particles are stable in water at pH 7, MES buffer at pH 6.5, and PBS at pH 7.4, and show a quite acceptable colloidal stability in cell medium supplemented with protein serum. The bare particles can also be functionalized by using a LbL approach with PAH and PAA, showing, however, less colloidal stability. Both YVO_4- and $GdVO_4$-based NPs show low cell toxicity, and can be used for biomedical applications, such as optical biolabels for imaging HeLa cells, and as biosensors, after an appropriate conjugation with analyte-sensitive dyes. Cell cytometry studies show that the uptake of YVO_4-based NPs by HeLa cells is faster than for $GdVO_4$-based ones. The influence of the particle size has also been evaluated, showing that smaller YVO_4-based NPs (51 nm) are taken up faster than their bigger counterparts (93 nm). Both types of luminescent NPs are dissolved at acidic pHs, *i.e.* pH 3.5, which offers a way for the NP excretion.

4. Experimental section

4.1 Materials

Yttrium(III) acetylacetonate hydrate ($Y(C_5H_7O_2)_3 \cdot xH_2O$ Aldrich, 99.95%, #438790), gadolinium(III) nitrate hexahydrate ($Gd(NO_3)_3 \cdot 6H_2O$, Aldrich, 99.99%, #451134) and europium(III) nitrate pentahydrate ($Eu(NO_3)_3 \cdot 5H_2O$, Aldrich, 99.9%, #207918) were selected as Ln precursors. Bismuth(III) nitrate pentahydrate ($Bi(NO_3)_3 \cdot 5H_2O$, Aldrich, 99.999%, #254150), and sodium orthovanadate (Na_3VO_4, Aldrich, 99.98%, #450243) were used as bismuth and vanadium sources, respectively. A mixture of ethylene glycol (EG, Fluka, >99.5%, #03750)–water was used as a solvent. Deionized water (ddH_2O, MilliQ® Academic, Millipore, Billerica, USA) with a resistance greater than 18.2 MΩ cm^{-1} was used for all experiments. For functionalization, polyacrylic acid (PAA, average M_w ~ 1800 Da, Aldrich, #323667), poly(allylamine hydrochloride) (PAH, average M_w ~ 17 500 Da, Aldrich, #283215), sodium chloride (NaCl, Roth, >99.9%, #HN00.2), Nile Blue A perchlorate (NB, Aldrich, 95%, #370088), and 1-ethyl-3-(3-dimethylaminopropyl) carbodiimide (EDC, Sigma-Aldrich, >98.0%, #03450) were employed. Different buffer media of biological interest were prepared from 2-(*N*-morpholino)ethanesulfonic acid hydrate (MES, Sigma, >99.5%, #M8250), Dulbecco's phosphate buffered saline without Ca^{2+} and Mg^{2+} (PBS, Biochrom, #L1825), fetal bovine serum superior (FBS, Biochrom, #S0615), Dulbecco's modified Eagle's medium–high glucose (DMEM, Sigma, #D1145), and Eagle's minimum essential medium (MEM, Sigma, #M5650). Hanks' balanced salt solution (HBSS, Sigma-Aldrich, #H8264), paraformaldehyde solution (8%, Electron Microscopy Sciences, #157-8-100), WGA (wheat germ agglutinin)-Alexa Fluor 488 (WCA 488, Oregon green, Invitrogen, #W6748), Hoechst reagent (Hoeschst 33342, trihydrochloride, trihydrate, Thermo Fisher, #H1399), lysosomal-associated membrane protein 1 (LAMP 1, mouse anti-human IgG1; the Developmental Studies Hybridoma Bank, University of Iowa, Department of Biology, USA, #H4A3, Supernatant), Dylight 649 (donkey anti-mouse IgG (H + L), secondary antibody, Jackson ImmunoResearch Laboratories, #715-605-150), glycine (Roth, #3908.1), saponin (Sigma-Aldrich, #S7900), bovine serum albumin (BSA, Jackson ImmunoResearch Laboratories, #001-000-161), trypsin/EDTA 0.05% solution (Gibco, Germany, #25300-054), and 4′,6-diamidino-2-phenylindole (DAPI, ThermoFisher, #D3571) were used for the fixation, staining and imaging of the cells, and for flow cytometry studies. All chemicals were used as received.

4.2 One pot synthesis and PAA functionalization of the Eu- and Bi-doped $REVO_4$ NPs

$Y(acac)_3$ (*i.e.* $(Y(C_5H_7O_2)_3 \cdot xH_2O)$, $Eu(NO_3)_3 \cdot 5H_2O$, and $Bi(NO_3)_3 \cdot 5H_2O$ were dissolved in EG in three different vials. To facilitate the dissolution of the reagents in EG, the solutions were mildly heated (~80 °C) under magnetic stirring. At the same time, Na_3VO_4 and PAA were dissolved in a mixture of water and EG. After cooling down to room temperature, appropriate amounts of the precursor solutions were mixed while continuing the magnetic stirring. The Eu/(Eu + Bi + Y) molar ratio was fixed to 8% in all the cases, while the Bi/(Eu + Bi + Y) molar ratio was varied from 0 to 20%. In the final solutions, the total [Y + Bi + Eu], and Na_3VO_4 concentrations were 0.02 M, and 0.1 M, respectively, while the PAA concentration was varied from 2 to 8 mg mL^{-1}. The final EG : H_2O volumetric ratio was 3.5 : 1.5. The so prepared solutions (final volume = 5 mL) were then aged for 5 h in tightly closed test tubes using an oven preheated at 120 °C. After aging, the resulting dispersions containing the precipitated NPs were cooled down to room temperature, centrifuged to remove the supernatants and washed twice with ethanol and once with distilled water (*i.e.* adding around 10 mL of the corresponding liquid, centrifuge and remove supernatants). Samples without PAA were also synthesized for LbL functionalization. Most of the NPs were dispersed in water, but some portions were dried in order to carry out further characterization. Eu- and Bi-doped $GdVO_4$ NPs were synthesized following the same protocol but using $Gd(NO_3)_3 \cdot 6H_2O$ as the Gd precursor. For these samples, the final PAA concentration was 2 mg mL^{-1}. A summary of the synthesized samples is shown in Tables 1 and S1.†

4.3 Layer-by-Layer functionalization with PAH and PAA

Different polyelectrolyte layers were deposited onto the surface of the non PAA-functionalized 8% Eu- and 20% Bi-doped $REVO_4$ NPs. The following positive and negative polyelectrolytes were used: poly(allylamine hydrochloride) (PAH, average M_w ~ 17500 Da), and polyacrylic acid (PAA, average M_w ~ 1800 Da). The first positive PAH layer was deposited as follows: 500 μL of an aqueous PAH solution (10 mg mL^{-1}, 0.05 M in NaCl, pH 6.5) were added to 150 μL of a water dispersion containing 0.5 mg of the NPs. The resulting dispersion was sonicated in cold water for 5 minutes and then shaken for 15 minutes. The so functionalized particles were washed three times with MilliQ water by centrifugation. For the deposition

Table 1 Experimental conditions for the synthesis of selected samples. Data corresponding to all the synthesised samples are shown in Table S1

Sample	$[Eu^{3+}]$ (M)	$[Bi^{3+}]$ (M)	$[Y^{3+}]$ (M)	$[VO_4^{3-}]$ (M)	PAA (mg mL^{-1})
Bi0YPAA	0.0016	0	0.0184	0.1	2
Bi20YPAA2	0.0016	0.004	0.0144	0.1	2
Bi20YPAA8	0.0016	0.004	0.0144	0.1	8
Bi20Y	0.0016	0.004	0.0144	0.1	0
	$[Eu^{3+}]$ (M)	$[Bi^{3+}]$ (M)	$[Gd^{3+}]$ (M)	$[VO_4^{3-}]$ (M)	PAA (mg mL^{-1})
Bi0GdPAA	0.0016	0	0.0184	0.1	2
Bi20GdPAA	0.0016	0.004	0.0144	0.1	2
Bi20Gd	0.0016	0.004	0.0144	0.1	0

Table 2 Morphological and colloidal characterization data of selected samples. DLS (number distribution) and ζ-potential measurements were recorded in water at pH 7. Errors are given in terms of standard deviations or in the case of the unit cell volume as absolute errors. N. r. = not recorded. Data corresponding to all the synthesised samples are shown in Table S2

Sample	Particle size (TEM) (nm)	Hydrodynamic diameter (nm)	Crystallite size (nm)	ζ-Potential (mV)	Unit cell volume (Å^3)
Bi0YPAA	88 ± 14	82 ± 3	62	−37 ± 2	319.24 ± 0.03
Bi20YPAA2	93 ± 7	108 ± 10	79	−42 ± 3	325.58 ± 0.02
Bi20YPAA8	51 ± 5	51 ± 2	57	−39 ± 2	325.61 ± 0.03
Bi20Y	107 ± 14	138 ± 7	N.r.	−19 ± 1	N.r.
Bi0GdPAA	39 ± 7	40 ± 2	53	−45 ± 1	330.32 ± 0.04
Bi20GdPAA	40 ± 8	41 ± 2	65	−41 ± 2	335.37 ± 0.02
Bi20Gd	51 ± 15	58 ± 4	N.r.	−25 ± 1	N.r.

of the second layer, 500 μL of an aqueous PAA solution (10 mg mL^{-1}, 0.05 M in NaCl, pH 6.5) were added, followed by 5 min of sonication and 15 minutes of shaking. Extra polyelectrolyte layers of alternate charge were deposited onto the NPs surface by following the same methodology. The final architecture was NPs@PAH@PAA@PAH.

4.4 Characterization

The particle morphology was examined by transmission electron microscopy (TEM, JEOL Model JEM 3010) operating at an acceleration voltage of 300 keV. High-angle annular dark-field imaging (HAADF) was carried out in a JEOL JEM 2200FS. Particle size distributions were obtained by counting about 100 particles from the TEM micrographs as recorded of particles in the dried state. By dynamic light scattering (DLS, Malvern Zetasizer Nano-ZS90) the size distribution of the NP suspensions in water (0.5 mg mL^{-1}) at pH 7 was recorded. The chemical composition of the NPs was studied by energy dispersive X-ray analysis (EDX) in a Bruker XFlash 5060 detector attached to the JEOL JEM 2200FS microscope. Bismuth, europium, yttrium, gadolinium, and vanadium contents were assessed by induced coupled plasma atomic emission spectroscopy (ICP-AES) using an ICP Horiba Jobin Yvon Ultima 2 spectrometer, for which the NPs were dissolved in concentrated HCl. The infrared spectra of the nanophosphors diluted in KBr pellets were recorded in a Jasco FT/IR-6200 Fourier transform infrared (FTIR) spectrophotometer. X-ray diffraction (XRD) studies were carried out using a Panalytical, X'Pert Pro diffractometer equipped with an X-Celerator detector. The crystallite size for several crystallographic directions (planes (101), (200), (112), (200), and (312)) of the tetragonal $REVO_4$ structures was determined by using the Scherrer formula. A value of 0.9 for the K shape factor was employed. Zeta (ζ) potential measurements of NP suspensions in water (0.5 mg mL^{-1}) at pH 7 were carried out in a Malvern Zetasizer Nano-ZS90 apparatus. The colloidal stability of the NP suspensions in different media (water at pH 7, 50 mM MES buffer at pH 6.5, PBS at pH 7.4, serum-supplemented (10% vol. fetal bovine serum) and serum free cell culture media) was monitored by analyzing the evolution of the hydrodynamic particle diameter with aging time, as measured by DLS. For these analyses the NP concentration was set to 0.5 mg mL^{-1}. Each measurement was repeated three times. The fluorescence emission and excitation spectra of the NPs in water suspensions (0.05 mg mL^{-1}) were measured on a PTI QuantaMaster™ spectrofluorometer (Photon Technology International) equipped with a 75 W xenon short arc lamp and the model 814 PTM detection system. Felix 32 software was used to collect and process the fluorescence data. The emission and excitation slit widths were both 2 nm. All optical measurements were made at room temperature, using a micro quartz cuvette of 10 mm light path. The photostability of the NPs was evaluated by analyzing the emission of immobilized NPs under continuous UV irradiation using a wide-field fluorescence microscope (Axiovert 200M, Zeiss, Germany).

4.5 Cell culture

Human cervical cancer cells (HeLa) were seeded and grown in Eagle's minimal essential medium supplemented with 10% fetal bovine serum (FBS), 1% L-glutamine and 1% penicillin/streptomycin. The cells were incubated at 37 °C in an atmosphere of 95% air and 5% CO_2.

4.6 Cellular uptake and imaging

HeLa cells were seeded in 8 well μ-ibidi plates (Ibidi #80826, 1 cm^2 per well) at a density of 15 000 cells per well. Each well was always filled with 300 μL of cell medium. After incubation for 24 h, their medium was replaced with fresh growth media containing the luminescent particles at a concentration of 25 μg mL^{-1}. After incubation for 24 h (37 °C and 5% CO_2), the samples were washed with HBSS (Hanks' Balanced Salt Solution), fixed with fixation solution (4% paraformaldehyde in PBS) for 15 minutes at room temperature, and washed three times with HBSS. Cell and nuclear membranes were stained with WGA (wheat germ agglutinin) conjugated with Alexa Fluor 488 (20 μg mL^{-1}), and Hoechst reagent (5 μg mL^{-1}) for 20 min at room temperature, respectively. In order to prove the intracellular location of the NPs, LAMP 1 (2 μg mL^{-1}) and Dylight 649 (4 μg mL^{-1}) were used as primary and secondary antibodies for immunostaining the lysosomal membranes. Samples were permeabilized with a permeabilization solution (5 mg glycine and 0.5 mg saponin/1 mL of PBS) for 5 minutes at room temperature, and then incubated at 37 °C with a blocking solution (20 mg BSA/1 mL of permeabilization solution) for 30 minutes. Cells were then incubated at 37 °C with a primary antibody (in blocking solution) for one hour, washed three times with the blocking solution and again incubated at 37 °C for one hour with a secondary antibody (in PBS; phosphate-buffered saline). Samples were washed three times with PBS before imaging. Imaging was performed with a wide-field fluorescence microscope (Axiovert 200M, Zeiss, Germany excitation filter for the NP visualization = 340 ± 24 nm, emission filter Long pass 600 nm).

For live imaging by using a visible laser radiation as the excitation source, HeLa cells were also seeded in 8 well μ-ibidi plates at a density of 10 000 cells per well, and were incubated with the luminescent NPs at a concentration of 10 μg mL^{-1} for 24 h. Cells (neither fixed nor immunostained) were washed 3 times and observed with a confocal laser scanning microscope (CLSM Meta 510, Zeiss, excitation diode laser 405 nm, emission band pass filter 604–754 nm). Further information on the microscope set up and used filters and lasers can be found in the ESI.†

4.7 Conjugation with Nile Blue

PAA-functionalized NPs doped with 8% Eu and 20% Bi were chosen for further conjugation with Nile Blue (NB) through a 1-ethyl-3-(3-dimethylaminopropyl) carbodiimide (EDC) mediated reaction. In a typical experiment, PAA-NPs (0.5 mg) and EDC (1 mL at 50 μM) were mixed and stirred for 10 min. Afterwards, NB solution (1 mL at 5 μM) was added and the mixture was incubated at room temperature overnight under gentle shaking. The mixture was further purified by centrifugation (10 000 rpm, 5 min) in order to separate the excess of reagents. The supernatant containing the not linked NB was discarded and the precipitate (functionalized NPs) was washed by adding 1 mL of water and stirring 10 min. Then, the NPs were again centrifuged (10 000 rpm, 5 min) and the same washing procedure was repeated three times. In the last washing, the supernatant had no colour, indicating that the free NB had been completely removed. The NB-PAA-NPs were finally dispersed in water at a final concentration of 0.5 mg mL^{-1}. A 20-fold dilution of the NB-PAA-NP solution (0.025 mg mL^{-1}) in the different buffer solutions was performed. Aqueous universal buffer solutions pH = 3–11 were prepared by mixing an appropriate volume of acidic and alkaline buffer components. The acidic buffer component comprised 0.04 M phosphoric acid, 0.04 M boric acid, and 0.04 M acetic acid, whereas the alkaline buffer component was 0.2 M sodium hydroxide solution. The resulting pH of the mixtures was measured using a pH meter (Crison pH Meter Basic 20). The fluorescence emission of the NB-PAA-NPs was recorded at different pH values (from 3 to 11) under two excitation wavelengths (342 and 600 nm). The ratiometric analytical signal, *i.e.* the fluorescence intensity at 622 nm (under 342 nm excitation) divided by the fluorescence intensity at 675 nm (under 600 nm excitation), was calculated for studying the pH response of the NPs.

4.8 Cytotoxicity assays and degradability

Cell viability assays were performed using a fluorescence-based approach employing resazurin. Resazurin is a non-toxic non-fluorescent compound, which in living cells is converted into fluorescent resorufin.[68] 7500 HeLa cells were seeded per well in a 96-well plate (100 µL medium per well, 0.32 cm^2 per well surface area, Corning) and incubated for 24 h. After 24 h, cells were washed with phosphate buffered saline (PBS), and the medium was replaced with fresh medium containing the PAA- and LbL-functionalized luminescent NPs in varying concentrations. After incubation again for 24 h, cells were washed with PBS and 10% of fresh resazurin solution in complete growth media was added. After 3.5 h of incubation with resazurin (37 °C and 5% CO_2) the samples were analysed with a fluorometer for the presence of resorufin, which is the reduced product of resazurin (excitation 560 nm, emission between 572 and 650 nm). The background emission (640–650 nm) was subtracted from each value of fluorescence emission. For evaluation the maximum fluorescence emission intensity of resorufin (580–590 nm) was used, which is assumed to correlate with the viability of the cells. Each measurement was repeated three times to obtain the mean values and the standard deviation. The normalized fluorescence intensity values were plotted against the NP concentrations. When possible, the LD_{50} of the NPs (defined as the lethal dose toxic for 50% of the cells under the given experimental conditions) was calculated from a fit with a sigmoidal curve (logistic dose response fit). Control experiments were performed with cells that were not incubated with NPs.

The dissolution of the NPs at acidic pH was studied by analyzing the evolution of the hydrodynamic particle diameter with aging time of NP suspensions (0.5 mg mL^{-1}) in MES 50 mM at pH 3.5 at room temperature (around 20 °C). Prior to the DLS measurements, the suspensions were sonicated for 10 minutes. DLS measurements were repeated three times.

4.9 Flow cytometry study

HeLa cells were seeded into 24-well plates (TPP, Switzerland, 1.86 cm^2 per well) with an amount of 40 000 cells per well with 700 µL of cell medium, and left overnight in an incubator at 37 °C and 5% CO_2. NPs were added to the cells (final concentration 10 µg mL^{-1}). The cells were incubated with NPs for 2, 4, 8, and 24 h. After incubation, the cells were washed 3 times with phosphate buffered saline (PBS, Biochrom) and detached with typsin/EDTA 0.05% solution. Trypsin was then neutralized with 400 µL of cell culture medium. Detached cells were transferred to FACS tubes (Falcon, Germany) and centrifuged at 250*g* for 5 minutes. The supernatant was removed and 500 µL of PBS were added. In order to discard the dead cells, 1 µL (1.1 mM) of 4′,6-diamidino-2-phenylindole (DAPI) was added to each tube. Resuspended cells with internalized particles were then analyzed with a flow cytometer (LSRFortessa) equipped with a genesis CX 355 STM compact laser system (UV laser 355 nm). In addition, three control measurements (cells without NPs, cells with DAPI, and dead cells with DAPI) were performed to exclude cell duplets and dead cells. The red fluorescence from the cells with internalized particles was measured by using a band pass 610/20 nm filter. The blue (BP 450/50 nm) fluorescence was also collected to discard dead cells in the counts. 10 000 events per sample were measured and every experiment was repeated 3 times. The mean red fluorescence intensity coming from the cells was calculated with FACSDiva software and plotted *versus* the time periods of incubation.

Acknowledgements

This work was supported by a Junta de Andalucía (Spain) Talentia Postdoc Fellowship, co-financed by the European Union's Seventh Framework Programme, grant agreement no 267226. Rocío Félix and Maximilian Schnabel are gratefully acknowledged for help with EDX and HAADF measurements, and sample preparation, respectively. CCC and SA acknowledge Alexander von Humboldt Foundation for a postdoctoral fellowship. Preliminary data corresponding to yttrium vanadate nanoparticles have been already shown in an extended abstract at the 2016 SPIE Photonic West conference.[29] Parts of this work were supported by the European Commission (grant FutureNanoNeeds to WJP), and by the Spanish Ministerio de Economía y Competitividad (project MAT2014-54852-R to MO). We acknowledge support of the publication fee by the CSIC Open Access Publication Support Initiative through its Unit of Information Resources for Research (URICI).

References

1 S. K. Murthy, *Int. J. Nanomed.*, 2007, **2**, 129–141.
2 S. Jiang, K. Y. Win, S. Liu, C. P. Teng, Y. Zheng and M.-Y. Han, *Nanoscale*, 2013, **5**, 3127–3148.
3 J. A. Barreto, W. O'Malley, M. Kubeil, B. Graham, H. Stephan and L. Spiccia, *Adv. Mater.*, 2011, **23**, H18–H40.
4 S. Ashraf, C. Carrillo-Carrion, Q. Zhang, M. G. Soliman, R. Hartmann, B. Pelaz, P. Del Pino and W. J. Parak, *Curr. Opin. Pharmacol.*, 2014, **18**, 98–103.
5 L. Y. Wang, R. X. Yan, Z. Y. Hao, L. Wang, J. H. Zeng, H. Bao, X. Wang, Q. Peng and Y. D. Li, *Angew. Chem., Int. Ed.*, 2005, **44**, 6054–6057.
6 F. Wang, W. B. Tan, Y. Zhang, X. P. Fan and M. Q. Wang, *Nanotechnology*, 2006, **17**, R1–R13.
7 D. K. Chatterjee, M. K. Gnanasammandhan and Y. Zhang, *Small*, 2010, **6**, 2781–2795.
8 Y. N. Xia, *Nat. Mater.*, 2008, **7**, 758–760.
9 S. Piana, M. Reyhani and J. D. Gale, *Nature*, 2005, **438**, 70–73.
10 A. P. Alivisatos, *Science*, 1996, **271**, 933–937.
11 J. Park, J. Joo, S. G. Kwon, Y. Jang and T. Hyeon, *Angew. Chem., Int. Ed.*, 2007, **46**, 4630–4660.
12 H.-X. Mai, Y.-W. Zhang, R. Si, Z.-G. Yan, L.-D. Sun, L.-P. You and C.-H. Yan, *J. Am. Chem. Soc.*, 2006, **128**, 6426–6436.
13 C. Feldmann, *Nanoscale*, 2011, **3**, 1947–1948.
14 X. H. Gao and S. M. Nie, *Trends Biotechnol.*, 2003, **21**, 371–373.
15 G. F. Wang, Q. Peng and Y. D. Li, *Acc. Chem. Res.*, 2011, **44**, 322–332.
16 H. Dong, S.-R. Du, X.-Y. Zheng, G.-M. Lyu, L.-D. Sun, L.-D. Li, P.-Z. Zhang, C. Zhang and C.-H. Yan, *Chem. Rev.*, 2015, **115**, 10725–10815.
17 C. Bouzigues, T. Gacoin and A. Alexandrou, *ACS Nano*, 2011, **5**, 8488–8505.
18 J. Chang, Y. Liu, J. Li, S. Wu, W. Niu and S. Zhang, *J. Mater. Chem. C*, 2013, **1**, 1168–1173.
19 N. Núñez, J. Sabek, J. García-Sevillano, E. Cantelar, A. Escudero and M. Ocaña, *Eur. J. Inorg. Chem.*, 2013, **2013**, 1301–1309.
20 A. Escudero, E. Moretti and M. Ocaña, *CrystEngComm*, 2014, **16**, 3274–3283.
21 N. O. Núñez, S. Rivera, D. Alcántara, J. M. De la Fuente, J. García-Sevillano and M. Ocaña, *Dalton Trans.*, 2013, **42**, 10725–10734.
22 M. Abdesselem, M. Schoeffel, I. Maurin, R. Ramodiharilafy, G. Autret, O. Clément, P.-L. Tharaux, J.-P. Boilot, T. Gacoin, C. Bouzigues and A. Alexandrou, *ACS Nano*, 2014, **8**, 11126–11137.
23 N. O. Núñez, P. Zambrano, J. García-Sevillano, E. Cantelar, S. Rivera-Fernández, J. M. De la Fuente and M. Ocaña, *Eur. J. Inorg. Chem.*, 2015, **2015**, 4546–4554.
24 D. Chen, Y. Yu, P. Huang, H. Lin, Z. Shan, L. Zeng, A. Yang and Y. Wang, *Phys. Chem. Chem. Phys.*, 2010, **12**, 7775–7778.
25 X. Y. Huang, J. X. Wang, D. C. Yu, S. Ye, Q. Y. Zhang and X. W. Sun, *J. Appl. Phys.*, 2011, **109**, 113526.
26 W. Xu, H. Song, D. Yan, H. Zhu, Y. Wang, S. Xu, X. Bai, B. Dong and Y. Liu, *J. Mater. Chem.*, 2011, **21**, 12331–12336.
27 S. Neeraj, N. Kijima and A. K. Cheetham, *Solid State Commun.*, 2004, **131**, 65–69.
28 U. Rambabu, N. R. Munirathnam, S. Chatterjee, B. S. Reddy and S. D. Han, *Ceram. Int.*, 2013, **39**, 4801–4811.
29 A. Escudero, C. Carrillo-Carrión, M. Zyuzin, R. Hartmann, S. Ashraf and W. J. Parak, *Proc. SPIE*, 2016, **9722**, 972202.
30 B. Yan and X. Q. Su, *J. Non-Cryst. Solids*, 2006, **352**, 3275–3279.
31 H. D. Nguyen, S. I. Mho and I. H. Yeo, *J. Lumin.*, 2009, **129**, 1754–1758.
32 Y.-C. Chen, Y.-C. Wu, D.-Y. Wang and T.-M. Chen, *J. Mater. Chem.*, 2012, **22**, 7961–7969.
33 Y. C. Chen, S. C. Huang, Y. K. Wang, Y. T. Liu, T. K. Wu and T. M. Chen, *Chem. – Asian J.*, 2013, **8**, 2652–2659.
34 S. Tanaka and S. Fujihara, *Langmuir*, 2011, **27**, 2929–2935.
35 B. N. Mahalley, S. J. Dhoble, R. B. Pode and G. Alexander, *Appl. Phys. A: Mater. Sci. Process.*, 2000, **70**, 39–45.
36 B. N. Mahalley, R. B. Pode and P. K. Gupta, *Appl. Phys. A: Solid Surf.*, 2000, **177**, 293–302.
37 I. Bertini and C. Luchinar, *NMR of Paramagnetic Molecules in Biological Systems*, Menlo Park, CA, 1991.
38 T. Pellegrino, S. Kudera, T. Liedl, A. Muñoz Javier, L. Manna and W. J. Parak, *Small*, 2005, **1**, 48–63.
39 N. T. K. Thanh and L. A. W. Green, *Nano Today*, 2010, **5**, 213–230.
40 S. Takeshita, T. Isobe, T. Sawayama and S. Niikura, *J. Lumin.*, 2009, **129**, 1067–1072.
41 S. Wilhelm, M. Kaiser, C. Wurth, J. Heiland, C. Carrillo-Carrion, V. Muhr, O. S. Wolfbeis, W. J. Parak, U. Resch-Genger and T. Hirsch, *Nanoscale*, 2015, **7**, 1403–1410.
42 Q. Wang, Y. Bao, X. Zhang, P. R. Coxon, U. A. Jayasooriya and Y. Chao, *Adv. Healthcare Mater.*, 2012, **1**, 189–198.
43 F. Wang, D. Banerjee, Y. S. Liu, X. Y. Chen and X. G. Liu, *Analyst*, 2010, **135**, 1839–1854.
44 Z. Wang, C. Liu, L. Chang and Z. Li, *J. Mater. Chem.*, 2012, **22**, 12186–12192.
45 F. Zhang, E. Lees, F. Amin, P. Rivera_Gil, F. Yang, P. Mulvaney and W. J. Parak, *Small*, 2011, **7**, 3113–3127.
46 G. B. Sukhorukov, E. Donath, S. Davis, H. Lichtenfeld, F. Caruso, V. I. Popov and H. Möhwald, *Polym. Adv. Technol.*, 1998, **9**, 759–767.
47 R. M. Fratila, S. G. Mitchell, P. Del Pino, V. Grazu and J. M. De la Fuente, *Langmuir*, 2014, **30**, 15057–15071.
48 G. B. Sukhorukov, D. V. Volodkin, A. M. Gunther, A. I. Petrov, D. B. Shenoy and H. Mohwald, *J. Mater. Chem.*, 2004, **14**, 2073–2081.
49 L. Wang, R. Yan, Z. Huo, L. Wang, J. Zeng, J. Bao, X. Wang, Q. Peng and Y. Li, *Angew. Chem., Int. Ed.*, 2005, **44**, 6054–6057.
50 E. Matijevic, *Chem. Mater.*, 1993, **5**, 412–426.
51 S. Rodríguez-Liviano, F. J. Aparicio, T. C. Rojas, A. B. Hungría, L. E. Chinchilla and M. Ocaña, *Cryst. Growth Des.*, 2012, **12**, 635–645.
52 A. Escudero, M. E. Calvo, S. Rivera-Fernández, J. M. De la Fuente and M. Ocaña, *Langmuir*, 2013, **29**, 1985–1994.

53 J. Wang, Y. Xu, M. Hojamberdiev, J. Peng and G. Zhu, *J. Non-Cryst. Solids*, 2009, **355**, 903–907.

54 A. K. Levine and F. C. Palilla, *Appl. Phys. Lett.*, 1964, **5**, 118–120.

55 L. J. Kirwan, P. D. Fawell and W. van Bronswijk, *Langmuir*, 2003, **19**, 5802–5807.

56 T. Katsumata, H. Takashima, T. Michino and Y. Nobe, *Mater. Res. Bull.*, 1994, **29**, 1247–1254.

57 R. D. Shannon, *Acta Crystallogr., Sect. A: Cryst. Phys., Diffr., Theor. Gen. Cryst.*, 1976, **32**, 751–767.

58 G. Schneider and G. Decher, *Langmuir*, 2008, **24**, 1778–1789.

59 Y. Liu, D. Tu, H. Zhu, E. Ma and X. Chen, *Nanoscale*, 2013, **5**, 1369–1384.

60 P. Rivera-Gil, D. Jimenez De Aberasturi, V. Wulf, B. Pelaz, P. Del Pino, Y. Zhao, J. M. De La Fuente, I. Ruiz De Larramendi, T. Rojo, X.-J. Liang and W. J. Parak, *Acc. Chem. Res.*, 2013, **46**, 743–749.

61 T. Cedervall, I. Lynch, S. Lindman, T. Berggård, E. Thulin, H. Nilsson, K. A. Dawson and S. Linse, *Proc. Natl. Acad. Sci. U. S. A.*, 2007, **104**, 2050–2055.

62 K. Riwotzki and M. Haase, *J. Phys. Chem. B*, 1998, **102**, 10129–10135.

63 D. C. Rodriguez Burbano, R. Naccache and J. A. Capobianco, in *Handbook on the Physics and Chemistry of Rare Earths*, ed. B. Jean-Claude and K. P. Vitalij, Elsevier, 2015, vol. 47, pp. 273–347.

64 F. Wang, J. A. Wang and X. G. Liu, *Angew. Chem., Int. Ed.*, 2010, **49**, 7456–7460.

65 S. Takeshita, H. Ogata, T. Isobe, T. Sawayama and S. Niikura, *J. Electrochem. Soc.*, 2010, **157**, J74–J80.

66 H. Hara, S. Takeshita, T. Isobe, T. Sawayama and S. Niikura, *Mater. Sci. Eng., B*, 2013, **178**, 311–315.

67 L. Kastl, D. Sasse, V. Wulf, R. Hartmann, J. Mircheski, C. Ranke, S. Carregal-Romero, J. A. Martínez-López, R. Fernández-Chacón, W. J. Parak, H.-P. Elsasser and P. Rivera-Gil, *ACS Nano*, 2013, **7**, 6605–6618.

68 J. O'Brien, I. Wilson, T. Orton and F. Pognan, *Eur. J. Biochem.*, 2000, **267**, 5421–5426.

69 L. Shen, *J. Funct. Biomater.*, 2011, **2**, 355–372.

70 M. Yu, S. H. Huang, K. J. Yu and A. M. Clyne, *Int. J. Mol. Sci.*, 2012, **13**, 5554–5570.

71 H. Herd, N. Daum, A. T. Jones, H. Huwer, H. Ghandehari and C.-M. Lehr, *ACS Nano*, 2013, **7**, 1961–1973.

72 B. Parakhonskiy, M. V. Zyuzin, A. Yashchenok, S. Carregal-Romero, J. Rejman, H. Mohwald, W. J. Parak and A. G. Skirtach, *J. Nanobiotechnol.*, 2015, **13**, 13.

73 I. Adjei, B. Sharma and V. Labhasetwar, in *Nanomaterial*, ed. D. G. Capco and Y. Chen, Springer, Netherlands, 2014, vol. 811, ch. 5, pp. 73–91.

74 M. Nazarenus, Q. Zhang, M. G. Soliman, P. Del Pino, B. Pelaz, S. Carregal-Romero, J. Rejman, B. Rothen-Rutishauser, M. J. D. Clift, R. Zellner, G. U. Nienhaus, J. B. Delehanty, I. L. Medintz and W. J. Parak, *Beilstein J. Nanotechnol.*, 2014, **5**, 1477–1490.

75 H. Meng, S. Yang, Z. Li, T. Xia, J. Chen, Z. Ji, H. Zhang, X. Wang, S. Lin, C. Huang, Z. H. Zhou, J. I. Zink and A. E. Nel, *ACS Nano*, 2011, **5**, 4434–4447.

76 B. D. Chithrani, A. A. Ghazani and W. C. W. Chan, *Nano Lett.*, 2006, **6**, 662–668.